JOURNAL OF MATERIALS SCIENCE 29 (1994) 4447–4459

Model for precipitation in polycrystalline Cu-11.55 at %–Be-0.23 at %–Co

C.R. HOUSKA
Department of Materials Science and Engineering, Virginia Polytechnic Institute and State University, Blacksburg, Virginia 24061, USA

The precipitate structure and matrix deformation were examined in a commercial Cu-11.55 at %–Be-0.23 at %–Co alloy by quantitative X-ray diffraction techniques. A model is proposed that is consistent with early electron microscopy results by Bonfield and Edwards [*J. Mater. Sci.* **9** (1974) 398] and recent advances by Khachaturyan and Laughlin [*Acta Metall. Mater.* **38** (1990) 1823]. Agreement was found for a precipitate model consisting of highly deformed versions of the equilibrium γ-phase. This is in accord with earlier results for γ'' and γ' precipitates and is further generalized to include the GP zone for this alloy. Two states of deformation are required, i.e. one relatable to γ'' and the GP zone, with a second relatable to a continuous deformation which describes the rotation of the γ' precipitate. The matrix becomes and remains severely deformed prior to and through the hardness maximum. Bragg-like matrix peaks become partitioned into three components: quasilines, static diffuse scattering and a residual Bragg peak. The so-called "arrowhead" scattering should be re-examined as a generalized form of Laue scattering, which includes a difference between the square of the scattering amplitudes for the precipitate and the matrix that it replaces.

1. Introduction

The details relating to the early stages of decomposition or ageing in a Cu-11.55 at % Be-0.23 at % Co alloy were examined as it approached maximum hardness. Emphasis is placed upon structural changes relating to the development of severe displacement fields about zones of decomposition. Considerable literature is available from electron microscopy and X-ray diffraction (XRD) data dealing with structural changes. These results provide a valuable information base for the interpretation of the XRD data in the present work and integrate well with our quantitative findings.

Age hardened copper–beryllium alloys investigated by XRD may be found in refs [1–6], and by transmission electron microscopy in refs [7–22]. This paper focuses on decomposition over what has been treated as the first two stages, i.e.

$$\text{supersaturated solid} \rightarrow \text{GP zones (or } \gamma'') \rightarrow \gamma' \quad (1)$$

which does not include the transformation to the equilibrium γ-phase. Much of the previous work was performed on binary Cu–Be alloys. It has been demonstrated [10, 23–25] that the addition of a small amount of cobalt ($\leqslant 0.3$ at %) does not significantly modify the continuous precipitation sequence. Consequently, results from similar binary alloys have provided a useful background for the present study.

The continuous precipitation process observed in the solution-treated and aged alloys [1] begins with the formation of GP zones. This is aided by the presence of a supersaturation of vacancies produced during the quench and is believed to be modified by the presence of cobalt [26]. A polycrystalline alloy containing a small amount of Co (or Ni) is somewhat easier to deal with experimentally than the binary for several reasons. First of all, some of the Co forms beryllides that retard grain growth in the parent phase. Large grains introduce statistical problems with respect to quantitative XRD intensities after a high temperature solution treatment, which is typically carried out between 780–800 °C. Also, the rate at which the continuous transformation proceeds is reduced so that the early stage can be examined with convenient ageing times and routine quenching techniques. A discontinuous transformation, i.e

$$\text{supersaturated} \rightarrow \alpha_x + \gamma^1$$

is also observed [26]. This nucleates at grain boundaries and grows into the adjoining grains. Structural and compositional changes associated with each new phase was found in regions immediately adjacent to the advancing interface. The kinetics of the reaction depended upon the growth of duplex cells, whereas the kinetics of continuous precipitation depended on the growth rate of individual precipitates. The precipitate orientation was not related to the grain into which it was growing, but rather had an orientation relationship with the supersaturated solid solution on the other side of the boundary. The presence of 0.28 wt % Co suppressed the discontinuous mode so that below 380 °C the major mode was continuous precipitation, whereas above 380 °C discontinuous precipitation predominated. After ageing below 380 °C, the cellular

reaction was confined to relatively small areas around the grain boundary. Since our primary interest is in the coherent continuous transformation, ageing was carried out below 380 °C. Diffraction patterns revealed that the discontinuous precipitate γ^1 had a B2 structure with $a = 0.27$ nm and a habit plane close to $\{1\,1\,3\}_\alpha$.

The presence of cobalt in copper–beryllium alloys retards continuous precipitation at ageing temperatures $\leqslant 350$ °C [11] thereby enabling an early stage of precipitation to be readily examined at temperatures as high as 315 °C. The hardness maximum corresponds to the formation of γ' as observed by an "arrowhead" structure present in electron diffraction patterns [26, 27]. This is followed by a slow decrease in hardness with further ageing time due to the coarsening of γ'. A broad hardness maximum was obtained for the ternary alloy after ageing the solution-treated material for 24 h at 315 °C (ca. 420 . . VHN), which extended over ca. 50 h.

The first observable feature of the decomposition of the supersaturated solid solution was the appearance of regularly oriented markings in the grains, which will be referred to as striations, along the traces of $\{1\,1\,0\}$ planes [26]. Striations associated with the GP zones resulted from a strain contrast effect. The striations were a rather diffuse basket-weave of light and dark contrast having a width and separation of 10 nm. Their density was quite high, and their distribution extremely uniform throughout the aged microstructure. An examination of many different areas of the polycrystalline foils allowed the following conclusions to be made regarding these structural features. The striations were parallel to $\{1\,1\,0\}$ traces. The striations revealed a net matrix contrast due to the strain fields of adjacent zones overlapping rather than the strain around an individual GP zone. The estimation of zone density was difficult as no individual GP zones were imaged; however, a value of $> 10^{24}\ m^{-3}$ was given.

As ageing proceeded the zones grew in size and the coherency of strain fields increased. Tyapkin and coworkers [6] proposed that the $\langle 1\,1\,0\rangle$ stubs, noted in X-ray studies of the early stages of ageing, were due to the anisotropy of the copper lattice. Tanner [14] and Sorokin [15] applied the same argument to the diffuse scattering and striations observed by electron microscopy. Each of the reciprocal lattice points possessed a specific number of $\langle 1\,1\,0\rangle$ stubs, e.g. three at $\{1\,1\,1\}$, four at $\{2\,0\,0\}$, five at $\{2\,2\,0\}$, etc. [14]. $\langle 1\,1\,0\rangle$ relrods at a given reciprocal lattice point were normal to the $\{1\,1\,0\}$ striations and GP zones on $(0\,0\,1)$ planes and produced strain contrast effects on $\{1\,1\,0\}$ planes at 45° to the zone. A diffuse basket-weave structure was observed after ageing for 30 min at 315 °C, with the diffuse striations lying along the traces of the $(1\,0\,\bar{1})$, $(0\,1\,1)$ and $(0\,1\,\bar{1})$, $(1\,0\,1)$ planes.

In the associated electron diffraction pattern from the matrix, two distinct types of relrods were present: namely long diffuse [0 0 1] relrods which passed through the reciprocal lattice points and the transmitted beam, and shorter, more intense stubs were present at reciprocal lattice points, but not through the transmitted beam. The [0 0 1] relrods were symmetrical about the reciprocal lattice points and the transmitted beam [26]. This type of scattering is related to the size of the plate-like precipitates formed on (0 0 1) matrix planes. It will be shown in a later section (Equations 2a and b), that it can be treated as a generalized Laue scattering. The relrod length was at least the reciprocal lattice distance from the origin to the (0 0 2) reflection, and can be taken approximately as a plane of unit cells forming a GP zone.

Plate-like precipitates were observed after ageing for 3 h at 315 °C. On further ageing, the striations became more diffuse. This progressive disintegration of the striations was accompanied by the formation of a second type of plate-like precipitate which was identified as the intermediate γ' precipitate. The original striations were still visible provided small plate-like precipitates, ca. 10 nm in diameter, were interspersed between them [26]. In a selected area diffraction pattern, curved reflections corresponding to a range of γ' orientations were observed. In addition, an important feature of the relrods was an intensity maximum along the relrod extending from d-spacings corresponding to $d = 0.36$ nm to $d = 0.27$ nm. No $\langle 1\,1\,0\rangle$ stubs were observed after the full transformation to the semi-coherent precipitate γ'.

A diffuse maximum was found to transform into a diffuse "arrowhead" which pointed toward the origin, with its "tip" at the position of the forbidden (0 0 1) matrix reflection. Its "base" at (0 0 4/3) corresponded to a d-spacing of 0.27 nm [26, 27]. The "arrowhead" was formed by the diffuse scattering from γ' precipitates having a wide range of orientations. This is relatable to a change in the habit plane. The "arrowhead" had its sides bounded by relrods along the $[\bar{1}\,1\,3]$ and $[1\,\bar{1}\,3]$ directions produced by precipitates with a range of habit planes from $\{0\,0\,1\}$ to $\{1\,1\,3\}$.

For longer ageing times, the diffuse interior of the "arrowhead" disappeared leaving two discrete relrods about the spacing of $d = 0.27$ nm along the $[\bar{1}\,1\,3]_a$ and $[1\,\bar{1}\,3]_a$ directions. No [0 0 1] relrods were present, suggesting a complete transformation to γ' giving a $\{1\,1\,3\}_a$ habit plane. Relrods were initially produced by thin γ' precipitates. On further ageing, two discrete diffraction spots were formed at $d = 0.27$ nm, which indicated that two variants of the γ' orientation were present.

A more recent theoretical paper by Khachaturyan and Laughlin [28] (KL theory), based largely on the electron microscopy of Rioja and Laughlin [27], introduced some interesting new thoughts on the transformations in the Cu–Be system. It was proposed that the γ'' and γ' phases are not transient metastable phases. Rather, they are precipitates of the equilibrium γ-phase subjected to elastic constraints imposed by the surrounding fcc matrix. The precipitate γ'' is epitaxial with (1 0 0) planes of the matrix, which forms layers of highly distorted B2 unit cells that are coherent with the surroundings. Their model assumes that the lattice parameters within the plane of cells are identical to those of the matrix. Since the lattice parameter for stress free or bulk γ (B2) is 0.27 nm and the corresponding distance in the matrix is 0.255 nm

compressive stresses are introduced. This leads to an incremental expansion of γ from 0.27 nm to 0.29 nm perpendicular to the plane of cells. The latter parameter was made to be in agreement with a reported value for the c-axis of γ'' by selecting appropriate elastic constants for the precipitate. The stress-free Bain strain, calculated from bulk lattice parameters ($a_\gamma = 0.27$ nm, $a_\alpha = 0.3612$ nm) is 0.0571 along each of two perpendicular axes within the (0 0 1) plane and -0.225 along the c-axis perpendicular to the plane. This leads to a tetragonal unit cell for γ''.

A second stage of decomposition is assumed to begin at the {0 0 1} platelets which further reduces the elastic energy. This was accomplished by a rotation of the habit plane from {1 0 0} to {1 1 2}. The model assumes that one of the axes of γ'' is invariant and remains at 0.255 nm during a diffusion controlled process yielding γ'. Rotation along one of the ⟨1 1 0⟩ directions, resulted in an increase in the second axis from 0.255 nm to 0.27 nm. Also, $c_{\gamma'}$ decreased from 0.29 nm to 0.281 nm as a result of the rotation. The final result predicts a monoclinic unit cell with lattice parameters already cited, and $\beta = 87.2°$. This deviation from a tetragonal cell is sufficiently small to be unresolved even in high resolution XRD. However, a monoclinic cell could lead to an apparent line broadening as a result of small peak separations. Although the KL model treats two states of elastic distortions of γ(B2) within a fcc lattice, the various classical designations remain convenient when relating to the diffraction data, i.e., GP zone or γ'' and γ'.

2. Overview of present X-ray diffraction results

X-ray diffraction (XRD) data, using monochromatic $CuK_{\alpha 1}$, radiation were collected with a position sensitive detector from samples aged at 315°C for 15 and 30 min, as well as for 3, 24 and 168 h. This temperature enabled a comparison with the electron microscopy results of Bonfield and Edwards [26] on a Cu base Telcon 250 alloy containing 11.50 at % Be and 0.30 at % Co. For the present research, a commercial Brush 25 alloy was used containing 11.55 at % Be with 0.23 at % Co. The similarity of compositions and thermal treatments allowed comparison with our results. All ageing treatments were carried out after a solution treatment in an argon atmosphere at 780°C for 15 min. Discs were cut initially from a hot extruded 0.875 diameter rod with a 3/32″ thickness and were quenched to room temperature in a brine solution. This treatment allowed a maximum grain size to develop which still permitted the XRD data to be statistically reproducible. Sample surfaces were acid cleaned and electro-polished prior to XRD measurements, and stored at −4°C between ageing treatments. A previous work describes the texture of the samples and related orientation factors due to the fibre texture processed into the rod [29].

A total time of 168 h resulted in some over-ageing (see Fig. 1). Ageing treatments of 3, 24 and 168 h were within 80% of a maximum hardness of 380 VHN. Samples aged for 15 and 30 min were in an earlier

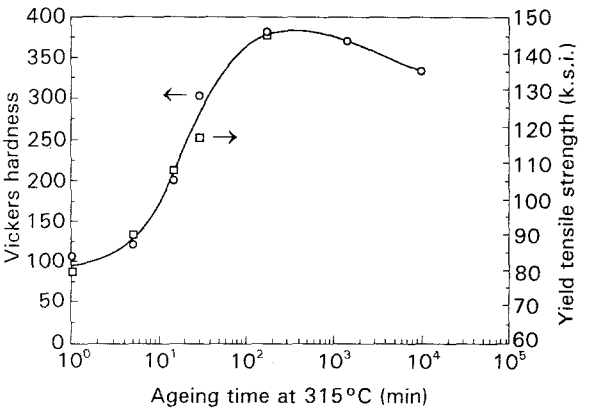

Figure 1 Hardness and yield strength with ageing time for Cu-11.55 at % Be-0.23 at % Co [30].

stage of transformation and involved GP or γ'', whereas for the three longer times the sample transformed to γ'.

Multiple order pairs, i.e. (1 1 1), (2 2 2) and (2 0 0), (4 0 0) matrix peaks are shown in Fig. 2 for all ageing treatments. Striking changes in shape and 2θ positions were observed in these selected combinations, as well as for other peaks not shown. These shape changes were examined in detail using the results of a diffraction theory, summarized in the next sections.

In relating to the electron diffraction photographs, which show diffuse stubs, the powder diffraction data contained an instrumental integration perpendicular to the diffraction vectors in reciprocal space. Although the integration did not allow separate stubs to be observed, the data are quantitative and enable powder diffraction theory to be applied more critically [31]. The high resolution of the $\kappa_{\alpha 1}$ diffraction optics, in most cases, allows one to distinguish between sharp and broad components (stubs) of the matrix diffraction peaks, which can go unobserved with electron diffraction over the range of ageing times employed. The broad peaks became more distinguishable at temperatures below 315°C due to additional shifts in 2θ.

In addition to the matrix peaks, data were obtained for {1 0 0} and {1 1 1} from continuous, discontinuous precipitates, as well as the corresponding beryllides (Fig. 3a and b). The latter phase has a B2 structure, like γ giving peaks that are sharp and fixed in their 2θ positions. These and all precipitate peaks were very weak but could be distinguished from the background with a position sensitive detector. Integrated intensities, lattice parameters and d-spacings for the precipitates are given in Tables I and II. The integrated intensities for the continuous and discontinuous peaks are essentially constant between 3 and 168 h. And, the relative intensity of the discontinuous precipitate represents only about 10% of the total from both precipitates. This is in accord with previous studies which found that discontinuous transformation was greatly reduced below 380°C.

Those (1 0 0) precipitate peaks which were first observed after 30 min of ageing had the diffraction vector parallel to a major dimensions of the precipitates while diffraction along the thin direction could not be

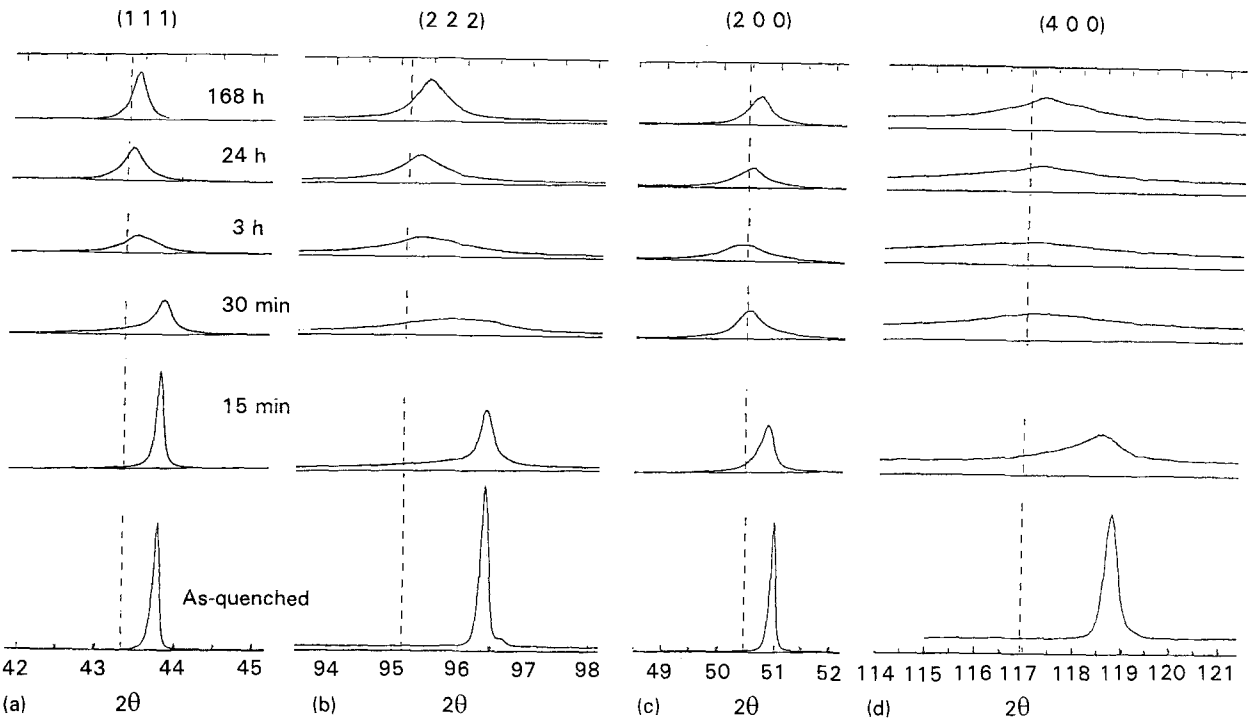

Figure 2 First- and second-order $CuK_{\alpha 1}$ matrix peaks from a Cu-11.55 at % Be-0.23 at % Co alloy aged for 15 min, 30 min, 3 h, 24 h and 168 h at 315 °C [30].

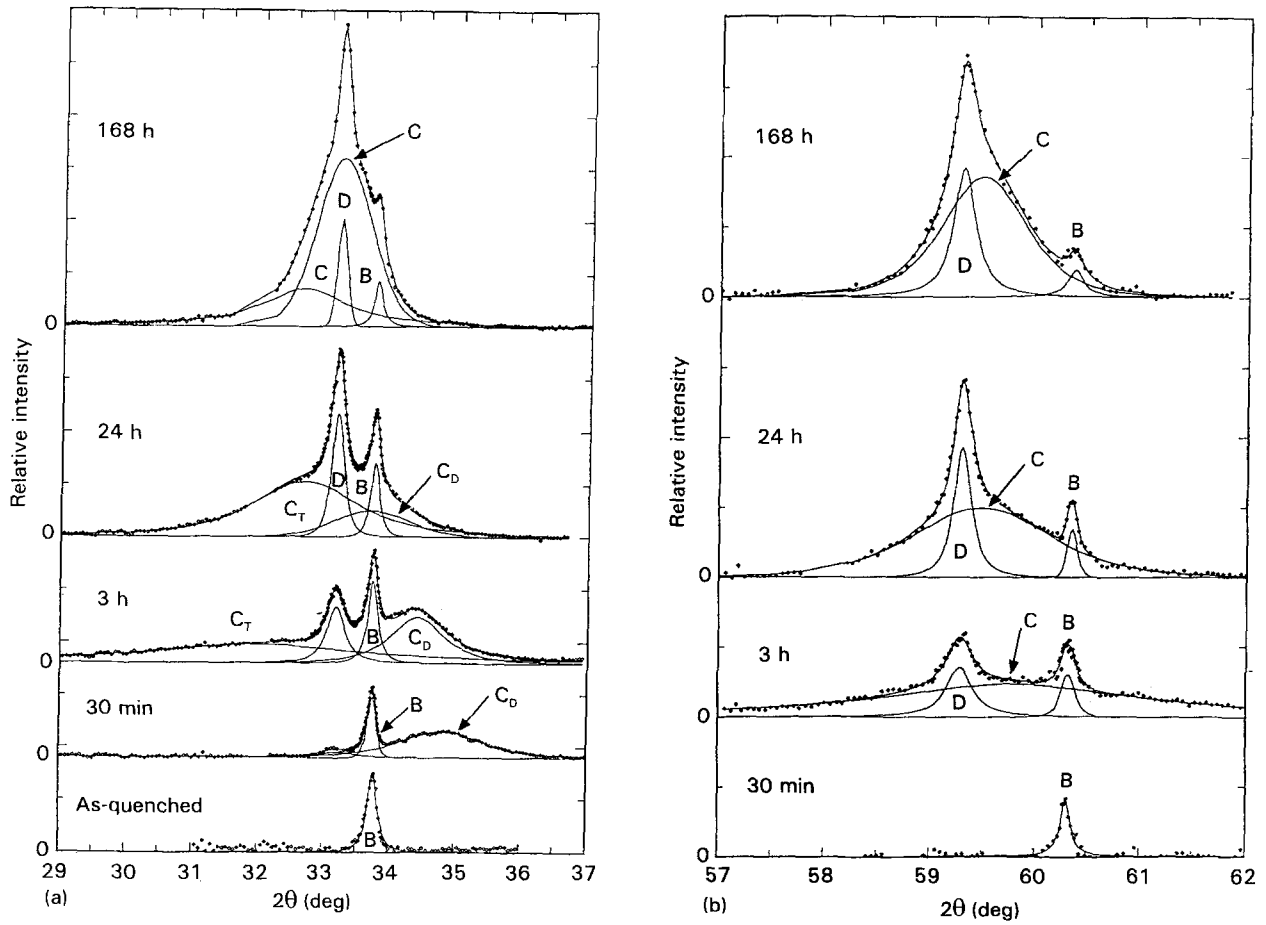

Figure 3 $CuK_{\alpha 1}$ diffraction peaks from aged Cu-11.55 at % Be-0.23 at % Co alloy [30]. (a) {1 0 0} peaks from continuous precipitate, where C_D is for (1 0 0) + (0 1 0) components and C_T is for (0 0 1). With 168 h ageing treatment, C_D and C_T were not separable, i.e. both C curves should be summed as one asymmetric curve. D and B designate γ' and beryllide, respectively. (b) {1 1 1} peaks from continuous precipitate, C; discontinuous, D; and beryllide, B. Solid curves are Pearson VII separations and the sum which relates to experimental points.

separated from the background. After 3 h (see Fig. 3a), a broad continuous precipitate peak was observed at $2\theta \approx 32.0°$, which shifted toward 33.24° with increasing ageing time. Similarly, the diffraction peak parallel to a major dimension also shifted continuously, but from 34.78° to 33.24°. The angle 33.24° corresponds to a cell edge of 0.2697 or 0.27 nm, the reported value for γ [28]. This corresponds to the edge length

TABLE I Lattice parameters in nm and integrated intensity data for the continuous precipitate at various times based upon a Pearson VII peak separation. c and a are tetragonal lattice constants, $d(1\,1\,1)$ = spacing from (1 1 1) peak position. $\langle c \rangle$ is the best estimate for the c-axis obtained from {1 0 0} and {1 1 1} peaks. Integrated intensities for the sharper (1 0 0) + (0 1 0), A_c(s); the broader (0 0 1) peak, A_c(B) and their sum A_c(T)

Time	Continuous						
(h)	c(0 0 1)	$\langle c \rangle$	a(1 0 0)	d_m(1 1 1)	A_c(T)	A_c(S)	A_c(B)
0.5	–	–	0.2577	–	–	–	–
3	0.2794	0.288	0.2602	0.1562	0.40	0.11	0.29
24	0.2736	0.275	0.2652	0.1553	0.33	0.07	0.26
168	–	(0.2693)	–	0.1553	0.50	–	–

TABLE II Lattice parameters and integrated intensity data (in nm) for the cubic discontinuous precipitate. Integrated intensity A_D, is summed from both the (1 0 0) and (1 1 1) peaks. The cubic lattice parameter for the beryllide is obtained from (1 0 0) and (1 1 1)

Time	Discontinuous			Beryllide	
(h)	a_D(1 0 0)	a_D(1 1 1)	A_D	a_B(1 0 0)	a_B(1 1 1)
3	0.2698	0.2698	0.051	0.2655	0.2656
24	0.2698	0.2697	0.066	0.2654	0.2654
168	0.2696	0.2697	0.041	0.2653	0.2654

for the Be-rich B2 structure of the discontinuous phase. The broad (1 1 1) peak (see Fig. 3b) shows a similar continuous downward shift but towards $2\theta = 59.48°$, which corresponds to a cubic lattice parameter of 0.2697 nm.

The data for 3 and 24 h did not allow a meaningful determination of a monoclinic cell because of overlap between (1 0 0) and (0 1 0) components of the sharper precipitate peak. However, the average as measured from the peak positions (see Table I) gives $a = 0.2602$ and 0.2652 nm for 3 and 24 h, respectively, which is comparable with the average value 0.2625 nm of the monoclinic cell obtained from KL theory. Their "c"-axis prediction ranged from 0.290 to 0.281 nm for γ'' transforming to γ'. This should be compared with 0.288 and 0.275 nm from this work. Perfect agreement is not expected because the elastic interaction between the matrix and precipitate, as well as the continuous nature of this transformation, was not completely treated in KL theory.

An analysis of particle size from the widths of the precipitate peaks was complicated by strain gradients and structural changes associated with habit plane rotation. The peak positions and half-widths for the matrix peaks over the 30 min to 168 h range are given in Table III. At this point, it is sufficient to note that there was a sharpening of the broadened matrix peaks and some tendency for shifting toward a higher angle for the longer times corresponding to the γ' transformation. This can also be seen in Fig. 2.

Table IV lists "apparent average particle sizes" calculated from the Scherrer Equation using a correction for instrumental broadening They are about an order of magnitude smaller than those reported by electron

TABLE III 2θ positions and half-widths of quasiline matrix peaks for (1 1 1), (2 2 2), (2 0 0) and (4 0 0) after long-term ageing compared with as quenched (AQ). All are in 2θ degrees

Time	(1 1 1)		(2 2 2)		(2 0 0)		(4 0 0)	
	2θ	Δ2θ	2θ	Δ2θ	2θ	Δ2θ	2θ	Δ2θ
AQ	43.75	0.09	96.39	0.15	50.96	0.12	118.79	0.31
30 min	–	–	96.00	0.97	50.50	0.78	117.19	3.02
3 h	43.47	0.50	95.39	1.36	50.39	1.03	117.15	2.57
24 h	43.43	0.30	95.33	0.79	50.52	0.75	117.15	2.33
168 h	43.49	0.24	95.46	0.61	50.67	0.48	117.20	1.93

TABLE IV Apparent average particle sizes L(S), L(B) and L(1 1 1) (in nm) using the Scherrer equation corrected for instrumental broadening after Pearson VII separation

Time	$\langle L(S) \rangle$	$\langle L(B) \rangle$	$\langle L(1\,1\,1) \rangle$
30 min	6.3	–	–
3 h	10.2	2.2	3.3
24 h	7.0	4.9	6.7
168 h	(10.0)		11.6

microscopy for ageing times extending over the $\gamma'' \rightarrow \gamma'$ transformation. This major discrepancy between these two findings is to be expected if γ' is monoclinic. Under these conditions, XRD line broadening contains an additional broadening due to the monoclinic distortions of the unit cell.

A quantitative examination of XRD profile data from samples aged for 15 and 30 min is given in the next section, using the elastic displacement field from ellipsoidal precipitates of finite size.

3. Diffraction theory

3.1. General comments

Diffraction theory has been developed for interpreting the X-ray scattering from randomly positioned precipitates in a finite, continuous crystalline matrix of fixed size [31]. No conditions are placed upon the severity of the displacements produced by precipitates. This theory may be used to describe the combined scattering from the matrix, with zones of severe distortion, as well as the scattering from precipitates. One arrives at the following conclusions:

1. The intensity of matrix scattering is partitioned into three components, i.e. Bragg, static diffuse (SD) and quasilines (Q). As the severity of the displacements increases, the intensity of the sharp Bragg peaks are systematically reduced, while the SD can, at first, increase to a maximum before vanishing like the Bragg peaks. Quasilines are much broader and increases in intensity with the volume fraction of a severely distorted zone.
2. When they are observable, the Bragg peaks retain their sharpness, which is determined by the overall size of the original matrix lattice. This is independent of the size or number of precipitates, as well as the severity of the field which surrounds them.
3. Scattering coherency from precipitates can influence the intensity from the matrix when the

structures of the precipitate and matrix are similar enough to introduce overlapping amplitudes of scattering.

4. In the mixed-partitioned state only two matrix peaks may be apparent, i.e. one appears sharp and a second broad. The sharp peak is a mix between the Bragg and SD, which tend to be located very near each other, while the broad one is largely quasiline. Consequently, matrix scattering may appear as a doublet.
5. Precipitate scattering includes direct scattering from the precipitate and the void region of the matrix where precipitates are located. A cross-term may become negligible when no overlap occurs between precipitate and void amplitude functions. Overlap and therefore a cross-term is expected between relrods resulting from the thin dimension of a disc precipitate. With the exception of relrod scattering, the shape of apparent precipitate scattering is typically determined by the size and shape of precipitates. Displacement fields from other precipitates can interact and produce additional broadening of the precipitate scattering. A peak shift and asymmetry resulting from strain may exist.

Quantitative X-ray diffraction analysis from samples containing a random mixture of two crystalline phases can be approached using well-established techniques [32]. However, when precipitation occurs within grains, several additional scattering effects are found. Voids are imagined to be filled with precipitates having a structure that in some way differs from the matrix. Lattice sites may not be conserved and an elastic disturbance in the matrix is included in the scattering amplitude, σ, as displacements that are obtained from an elastic model. The amplitude, σ_v, is a summation over fictitious matrix cells that are subtracted to make space for an average precipitate, and σ_β is a summation over average precipitate cells occupying an average void having a structure factor, F_β. The total number of matrix cells, with structure factor, F, before any precipitation, is N. Precipitate lattice parameters are a_1^β, a_2^β, and a_3^β, with reciprocal axes b_1^β, b_2^β, and b_3^β. Combining amplitudes and squaring gives the single crystal intensity per cell

$$\frac{I}{N} = F_{MP}^2 \frac{\sigma^2}{N} + C_v(1 - C_v)\frac{1}{N_v}(F_\beta \sigma_\beta - F\sigma_v)^2, \quad C_v < 0.5 \tag{2a}$$

$$C_v = \frac{n_v N_v}{N}$$

where n_v = the number of voids or precipitates and N_v is the average number of matrix atoms removed (or replaced) per precipitate and

$$F_{MP} = F\left\{1 + \frac{C_v}{N_v}\left[\left(\frac{F_\beta(M)}{F}\right)\sigma_\beta(M) - \sigma_v(M)\right]\right\} \tag{2b}$$

The structure factor, for the matrix F_{MP}, is altered if the scattering amplitude of the precipitate has a non-zero value at the Bragg peak for the matrix. The degree of overlap determines the coherency at the sharp Bragg peak originating from the matrix due to precipitate scattering. It also includes a negative contribution from the fictitious matrix cells in that volume occupied by precipitates. The second term in Equation 2a, when expanded as a binomial, contains relatively broad Bragg scattering from the precipitate, void scattering and a cross-term. It reduces to the classical Laue monotonic diffuse scattering if the precipitates contain only one atom, B, in a matrix of A atoms.

The two reciprocal lattices, i.e. one for the matrix and a second for the precipitate, are typically related by orientation relationships. Orientation relationships, differences in the reciprocal lattice vectors and the ratio $C_v F_\beta(M)\sigma_\beta(M)/N_v F\sigma_v(M)$ determine the coherency correction contained in F_{MP}.

For the present alloy, with scattering directions parallel to a large dimension of the precipitate, the precipitate size and the lattice are sufficiently large and different so that there is no significant overlap causing $\sigma_\beta(M) = \sigma_\beta\sigma_v = 0$. This gives the following simplified form

$$\frac{I}{N} = F^2\left(1 - C_v\frac{\sigma_v(M)}{N_v}\right)^2\left(\frac{\sigma^2}{N}\right) + C_v(1 - C_v)\left[\frac{(F_\beta\sigma_\beta)^2}{N_v} + \frac{(F\sigma_v)^2}{N_v}\right], C_v < 0.5 \tag{3}$$

and represents a departure from that typically used in a conventional quantitative phase analysis due to a void correction and the more complicated forms for σ^2, σ_β^2 and σ_v^2 when displacements are present.

3.2. Scattering from highly distorted lattices with precipitates

Lattice distortion associated with precipitation can become severe and produce special scattering effects. Thus far, no quantitative verification between theory and experimental data are available when precipitates produce severe matrix distortions which encompass a significant volume fraction of the matrix. For powder diffraction, one considers pairs of cells of height a_3 within columns perpendicular to the Bragg planes [33]. With cubic systems, their interplaner spacing d is given by

$$d = \frac{a}{(h^2 + k^2 + l^2)^{1/2}} = \frac{a_3}{l_o} \tag{4}$$

where (hkl) represent the normal Miller indices for the lowest order ($l_0 = 1$) and sets of planes of like orientation. a_3 is determined from the lattice parameter, a, of the normal cubic cell and the indices h, k and l. Higher orders are designated by $(n_o h, n_o k, n_o l)$ with $l_o = n_o$. The basic unit of distance along a column, $d = a_3$, determines $(m_3 - m_3')a_3$, the separation distance between nth neighbour pairs of cells at $m_3 m_3'$. All distances and displacements entering into the intensity calculations become projected along specified columns normal to the reflecting planes. The location of the undisplaced origin of the unit cell at $m_1 m_2 m_3$ is given by

$$R(m) = m_1 a_1 + m_2 a_2 + m_3 a_3 \tag{5}$$

which has an unprojected displacements of

$$\mu(m) = X_m a_1 + Y_m a_2 + Z_m a_3 \tag{6}$$

where m designates the location given by Equation 5.

A displacement calculation is outlined in ref. [34] for an ellipsoidal precipitate. When severe displacements are included, one finds [31]

$$\frac{\sigma^2}{N} = e^{-2M_s}\left\{\sum_n \left(\frac{N_n}{N_3}\right) e^{2\pi i n h_3} + \sum_n \left(\frac{N_n}{N_3}\right)[e^{\phi(n)} - 1 - \phi(n)]\, e^{2\pi i n h_3} + \sum_n \left(\frac{N_n}{N_3}\right)\phi(n)\, e^{2\pi i n h_3}\right\} \tag{7a}$$

which requires a summation over nth neighbour cells in columns having an average height of N_3.

The transform of $\phi(n)$ is given by

$$\phi(h_3) = \sum_n \phi(n)\, e^{2\pi i n h_3} = X_c\left\{\sum_{m_1}\sum_{m_2}\sum_{m_3}[e^{2\pi i l_0 Z_{m_3}} - 1]\, e^{2\pi i m_3 h_3'}\right\}^2 \tag{7b}$$

and

$$2M_S = \phi(n=0) = X_c \sum_{m_1}\sum_{m_2}\sum_{m_3}[1 - \cos(2\pi l_0 Z_{m_3})] \tag{7c}$$

In dealing with experimental powder pattern shape functions, measured along the 2θ axis, the intensity scaling from a diffractometer is somewhat modified according to [31]

$$K_{os}\, K_{is}(2\theta) \tag{8a}$$

with

$$K_{is}(2\theta) = \frac{I_0 A w h}{\mu V_c^2 d}\,\frac{1 + P\cos^2 2\theta}{(1+P)\sin^2\theta}\, j g_i e^{-2(M_T + M_{os})} \tag{8b}$$

and

$$2M_{OS} = D_1 X_B (1 - X_B)\left(\frac{1+\nu}{1-\nu}\right)^2 V_{SF}^2 (h^2 + k^2 + l^2) \tag{8c}$$

The constant K_{os} is not of interest, since only relative intensities are of importance. Other terms are: I_o = intensity of incident beam, A_0 = cross-sectional area of incident beam at the specimen, w and h are the receiver-slit width and height, respectively; μ is the overall linear-absorption coefficient of the alloy; V_c is the volume of an average unit cell in the matrix; j is the multiplicity factor of the normal Bragg peak; g_i is the orientation correction factor for planes i if the sample has a texture ($g = 1$ if the sample is an ideal powder); P is the polarization factor*, which is one if no monochromator is used; 2θ is the diffraction angle for each of the three components for matrix scattering. Typically, the peak separation between the three components is small enough to take a common constant $K_{is}(2\theta)F_{MP}^2$ for all three components at each (hkl) peak. M_T is commonly calculated from Debye theory [33] and M_{OS} for a dilute solution of unclustered random atomic point-like defects is given by Equation 8c. This assumes that for the present Cu–Be–Co alloy two distributions of Be exist. For the parent, the distribution is depleted in Be and tends to be monoatomic while for Be already located in precipitates it is highly clustered and leads to relatively severe distortions. If the value of M_{OS} is taken for as quenched samples, it is found to be a fraction of the thermal term M_T and can be neglected. The M_S term found to be associated with precipitates is dominant and determines the redistribution of matrix intensities. The Krivoglaz Equation (Equation 8c) can be evaluated with $D_1 = 0.0587$ for fcc and 0.0932 for bcc lattices [35]. Here X_B is the atomic fraction of atom type B in the matrix, ν = Poisson's ratio, $V_{SF} = 1/v\ \partial v/\partial X_B$ is the volume size factor for B atoms dissolved in an A-lattice [36].

The powder pattern describing the shape of the matrix intensity distributions, scaled by Equation 8a, is combined with Equation 7a giving the Bragg, static diffuse and quasiline contributions, respectively:

$$\frac{P_M(2\theta)}{K_0 e^{-2M_s}} = K_{is}(2\theta_B)F_{MP}^2 \sum_n \left(\frac{N_n}{N_3}\right) e^{2\pi i n h_3} + K_{is}(2\theta_{SD})F_{MP}^2 \sum_n \left(\frac{N_n}{N_3}\right)\phi(n) e^{2\pi i n h_3} + K_{is}(2\theta_Q)F_{MP}^2 \sum_n \left(\frac{N_n}{N_3}\right) \times [e^{\phi(n)} - 1 - \phi(n)]\, e^{2\pi i n h_3} \tag{9}$$

Relative integrated intensities for these parts are given by:

1. Bragg e^{-2M_s} (10a)
2. Static diffuse $2Me^{-2M_s}$ (10b)
3. Quasiline $1 - e^{-2M} - 2Me^{-2M_s}$ (10c)

which are determined by $2M_S$ or $\phi(n=0)$ according to Equation 7c.

Equation 10a–c may be used without additional scaling if the relative integrated intensities from individual (hkl) distributions are examined separately. However, if different peaks are to be inter-related, the scaling factor of Equation 8a is replaced by [31]

$$K_0 K_i(2\theta), \tag{11a}$$

with

$$K_i(2\theta) = (I_o A_o w h/\mu V_c^2) \times [(1 + P\cos^2 2\theta)/(1+P)\sin^2\theta\cos\theta]\, j g_i e^{-2(M_T + M_{os})}. \tag{11b}$$

3.3. Precipitate scattering

In the general case where precipitate and void scattering overlap, the intensity distribution may not be

*If P is not known from experiment, it is taken to be $\cos^2 2\theta'$, where $2\theta'$ = diffraction angle from the monochromator.

clearly distinguishable as separate peaks. The relrod scattering described previously is such an example. It has the form of the classical Laue monotonic scattering, but instead of dealing merely with the difference in scattering from two kinds of atoms, one takes a difference in amplitude from atoms arranged into precipitates and a similar but fictitious zone of matrix atoms. The latter look like an arrangement of matrix atoms extending over those distances required to form a void. Their positions and composition are defined in terms of the matrix atoms and its lattice. The local strain conditions are those existing in the matrix which develop as a result of precipitation. This likeness with the matrix causes void intensity to overlap with that of the matrix. Furthermore, with the dominance of particle size broadening, a separation into its diffuse components according to Equation 9 is not useful. For the early states of precipitation, it is reasonable to expect displacement fields to be continuous through each precipitate. However, each precipitate is subjected to an additive transformation strain that is not directly imposed upon a void. This additional transformation strain introduces a new lattice both in real and reciprocal space. The direct void and precipitate intensities may be simply written in the form

$$\frac{I_x}{N} = C_v(1 - C_v)F_x^2 \frac{e^{-2M_s}}{N_v} \sum_{n_x} \left(\frac{N_n}{N_3}\right) e^{\phi(n)} e^{2\pi i \mathbf{h}\cdot\mathbf{r}} \qquad (12)$$

with x referring to either voids or a precipitates. These intensities appear in Equation 2a along with a third cross-term which requires both void and precipitate amplitudes. This, of course, vanishes to give Equation 3 when the overlap becomes insignificant.

3.4. Displacements in matrix

The calculation of both $\phi(n)$ and $2M$ require a model for the displacement field produced by precipitates experiencing a misfit with the matrix. Elastic anisotropy must be considered in treating a dilute Cu base lattice. An ellipsoidal precipitate is used because of the large range of shapes that can be treated, including a flattened ellipsoid which approximates a thin disc.

These are similarities and differences with respect to the previously discussed model proposed by Khachaturyan and Laughlin [28]. Both begin with a tetragonal stress-free Bain strain described by

$$\varepsilon_{ij}'^{T} = \begin{bmatrix} 0.0554 & 0 & 0 \\ & 0.0554 & 0 \\ & & -0.2537 \end{bmatrix}$$

with

$$\varepsilon_{11}'^{T} = \varepsilon_{22}'^{T} = \frac{a_\gamma - a_\alpha/\sqrt{2}}{a_\alpha/\sqrt{2}},$$

$$\varepsilon_{33}'^{T} = \frac{a_\gamma - a_\alpha}{a_\alpha}, \qquad (13)$$

$$\varepsilon_{12}'^{T} = \varepsilon_{13}'^{T} = \varepsilon_{23}'^{T} = 0$$

and $a_\alpha = 0.3615$ nm and $a_\gamma = 0.2698$ nm. For the KL model, it is assumed that planar atoms in the precipitate fit exactly with the (1 0 0) planes of the matrix. In the present work, this is not assumed. Instead, flattened ellipsoidal precipitates interact elastically with the matrix along all three tetragonal axes. The equivalent matrix transformation strain contains precipitate size and shape which enter into the Green function formulation of the displacements as scaling factors.

It is convenient to have an estimate as a starting point for an equivalent transformation strain which acts on the matrix material. This is defined in terms of the following operations:

1. Cut the region to be transformed out of the embedded matrix.
2. Let the cut out region transform without the elastic constraints imposed by the matrix. The strain with respect to the original matrix, obtained under this condition, is called the stress-free transformation strain.
3. Apply surface forces to the transformed region to restore its original form.
4. Put the region with the applied forces back into the matrix.
5. Assert another set of surface forces that are equal and opposite to the forces applied in (3) and let the system (matrix and transformed region) deform under the latter applied forces according to the theory of elasticity. Equivalent forces are established that act on matrix material and this provides an equivalent transformation strain.

A set of elastic constants are assumed [30] for the precipitate such that: the precipitate is elastically stiffer, and there is agreement with the observed habit for elastically constrained γ [between (1 1 2) and (1 1 3)]. These have been chosen as

$$\begin{aligned} c'_{11} &= 2.70 \times 10^{11}\ \mathrm{N\,m^{-2}} \\ c'_{12} &= 1.55 \times 10^{11}\ \mathrm{N\,m^{-2}} \\ c'_{44} &= 1.50 \times 10^{11}\ \mathrm{N\,m^{-2}} \end{aligned} \qquad (13a)$$

and those for the matrix are already known from experiment [37], i.e.

$$\begin{aligned} c_{11} &= 1.70 \times 10^{11}\ \mathrm{N\,m^{-2}} \\ c_{12} &= 1.225 \times 10^{11}\ \mathrm{N\,m^{-2}} \\ c_{44} &= 0.758 \times 10^{11}\ \mathrm{N\,m^{-2}} \end{aligned} \qquad (13b)$$

The equivalent stress-free transformation strain is found to be

$$\varepsilon_{ij}^{T} = \begin{bmatrix} 0.1124 & 0 & 0 \\ 0 & 0.1124 & 0 \\ 0 & 0 & -0.3518 \end{bmatrix} \qquad (14)$$

The sum of the diagonal terms give a fractional volume change of -0.2540 per Be atom for the 50 at % Be γ-phase in a dilute fcc solution. This agrees well with the volume size factor of -0.265 for Be in pure Cu [36]. An ellipsoid with semi-axis $A_1 = A_2 = 4.0$ nm and $C = 0.175$ nm were used for this calculation.

Fig. 4a and b illustrate first quadrant equi-displacement contours for a (0 0 1) ellipsoid with $A_1 = A_2 = 3.50$ nm, $C = 0.60$ nm and $\varepsilon_{11}^{T} = \varepsilon_{22}^{T}$

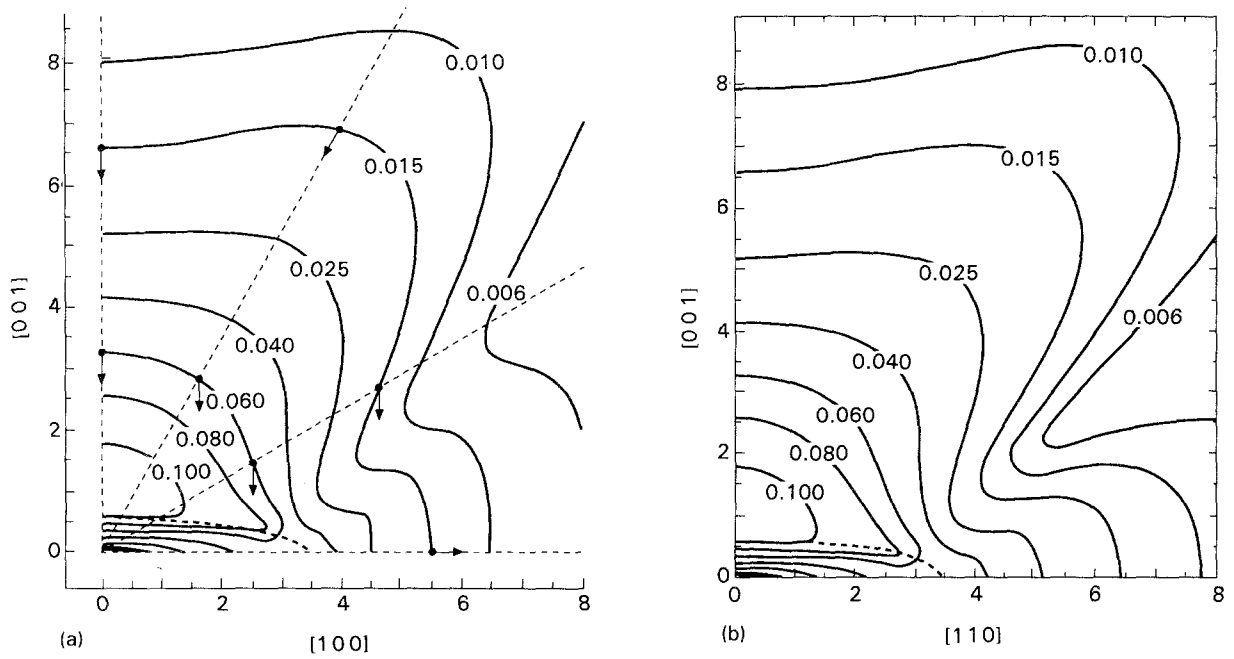

Figure 4 (a) Equi-displacement contours on (0 1 0) plane for an ellipsoidal defect with $a = b = 3.5$ nm and $c = 0.6$ nm, $\varepsilon_{11}^T = 0.112$ and $\varepsilon_{33}^T = -0.334$. The flat face of the ellipsoid is lying on the (0 0 1) plane. Displacement directions are shown in 0.060 and 0.015 nm contours [30]. (b) Same conditions as (a) but equi-displacement contours are on (1 $\bar{1}$ 0) plane [30]. All numbers are in nm.

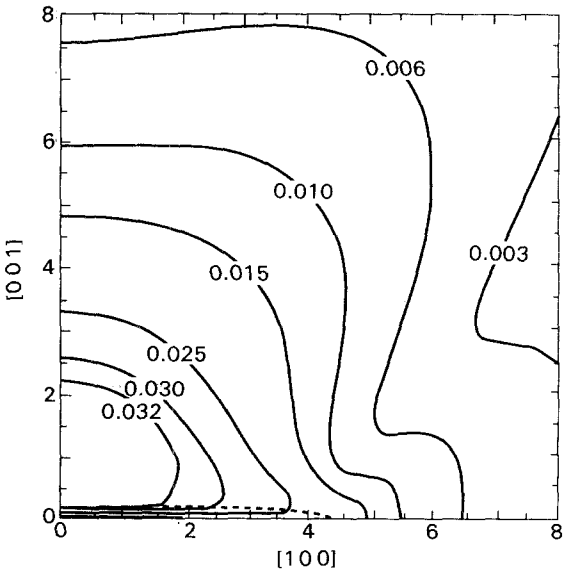

Figure 5 Equi-displacement contours on (0 1 0) plane for an ellipsoidal defect with $a = b = 4.5$ nm and $c = 0.19$ nm, $\varepsilon_{11}^T = \varepsilon_{22}^T = 0.112$ and $\varepsilon_{33}^T = -0.334$. The flat face of the ellipsoid is lying on the (0 0 1) plane. All numbers are in nm [30].

$= 0.112$, $\varepsilon_{33}^T = -0.334$ in a Cu matrix. Fig. 4a is a section of the (0 1 0) plane, while b is in a (1 1 0) plane. The displacements in the plane of the ellipsoid become extended along the $\langle 1\,1\,0 \rangle$ directions by ca. 20%. This tendency also exists for the [1 0 1] and along [1 1 1], as seen in Fig. 4b. At large distances, the field tends to become radial and appears to have a butterfly wing at ca. 35°. Fig. 4a illustrates the direction of the vector displacements for 0.6 and 0.15 equi-displacement contours. As expected, the vector rotates from an inward displacement along the "c" axis of the ellipsoid to an outward direction in the plane of the ellipsoid. Fig. 5 illustrates the field used to fit a sample aged at 315 °C for 15 min.

The field of a circular disc simulated under like conditions appeared very similar to that of the flat ellipsoid of revolution. One difference is the final strain inside a circular disc is not constant as it is for an ellipsoid. This can have some bearing on the XRD broadening from a disc-shaped precipitate.

The projected displacements are inserted into Equation 7b to determine $\phi(n)$ and $2M$. These terms were averaged over all three distinguishable variants of $\{1\,0\,0\}$ planes.

4. Computer simulations – γ″

4.1. Matrix

A detailed analysis was carried out for samples aged at 315 °C for 15 and 30 min using Equation 9. According to classical definitions, these contain GP and γ″, respectively; however, both may be described with a $\{1\,0\,0\}$ habit plane. Matrix composition was obtained using the metastable diagram for the binary Cu–Be alloy [38]. These values range from ca. 9 to 4 at % Be depending upon whether GP or γ″ limits are taken. Intermediate values of 8 and 6 at % Be were found to be in agreement with the data. The sharp

TABLE V Parameters used to calculate diffraction profiles

Sample condition	Equivalent transformation strain	Matrix composition	Site probability, X_c	Defect dimension (nm)
Aged for 15 min at 315 °C	$\varepsilon_{11}^T = 0.112$ $\varepsilon_{22}^T = 0.112$ $\varepsilon_{33}^T = -0.334$	8%	4.49×10^{-5}	$a = 4.5$ $b = 4.5$ $c = 0.19$
Aged for 30 min at 315 °C	$\varepsilon_{11}^T = 0.128$ $\varepsilon_{22}^T = 0.128$ $\varepsilon_{33}^T = -0.368$	5%	6.74×10^{-6}	$a = 10.0$ $b = 10.0$ $c = 0.5$

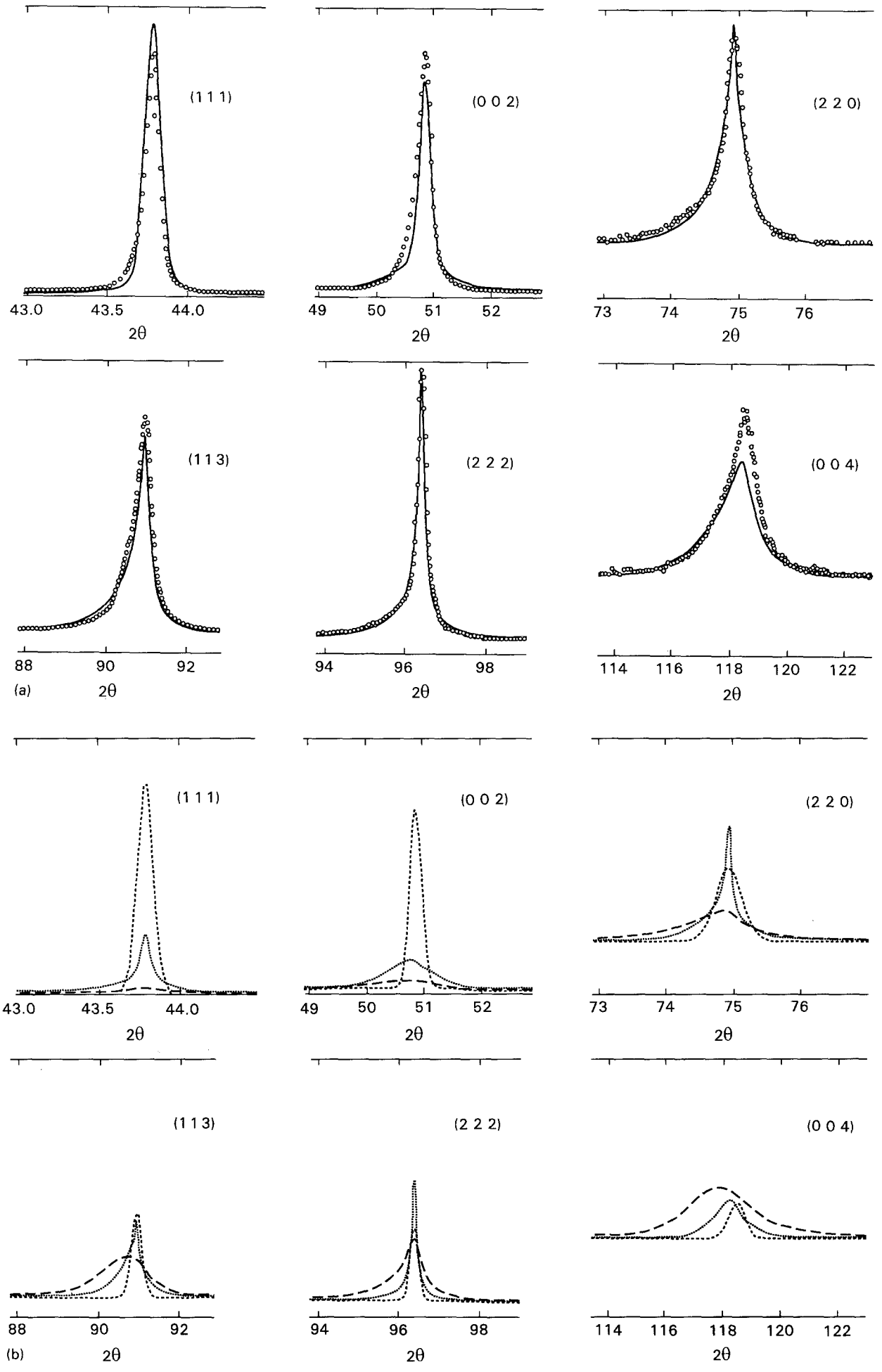

Figure 6 (a) Full set of data points for a Cu-11.55 at % Be-0.23 at % Co alloy aged 15 min at 315 °C using $CuK_{\alpha 1}$ radiation. Solid curve was calculated from model and contains Bragg, SD and Q. (b) Illustrates individual Bragg (points), SD (intermediate dash) and Q (large dash) calculations used as sum in (a).

TABLE VI Calculated $2M_S$ values for samples aged for 15 and 30 min at 315 °C

Peaks	$2M_S$ (15 min)	$2M_S$ (30 min)
1 1 1	0.463	5.509
0 0 2	0.605	6.647
2 2 0	1.224	13.46
1 1 3	1.650	16.76
2 2 2	1.817	19.63
0 0 4	2.270	24.13

Bragg peaks were fitted with Gaussian functions having half-maximum widths of 0.07, 0.15, 0.24, 0.20, 0.15 and 0.40° for the (1 1 1), (0 0 2), (2 2 0), (1 1 3), (2 2 2) and (0 0 4), respectively. Because the Gaussians are symmetrical functions, a small low angle asymmetry due to the axial divergence in the XRD optics is not fitted in the simulations for the (1 1 1) and (2 0 0). Equivalent transformation strains and ellipsoidal dimensions are given in Table V for ellipsoids having the 50 at % Be composition of the γ-phase. Computer simulations for the powder pattern are illustrated in Fig. 6a and b, with a giving the experimental points along with the theoretical. Fig. 6b shows the partitioning into Bragg, SD and quasiline components. Partitioning is determined by $2M_S$, as given in Table VI, according to Equation 10a–c. For the 30 min ageing treatment, $2M_S$ is large for all values of (*hkl*), such that the powder pattern consists mainly of shifted and broadened quasilines (see Fig. 2). A re-examination of Table V shows a thickening of the plate-like precipitates as the ageing time increases to 30 min, as well as an increase in diameter from 9.00 to 20.00 nm. The equivalent transformation strains show only a small (ca. 10%) increase with increasing precipitate size and are larger in magnitude than the Bain strains (Equation 13) calculated from the lattice parameters of the unstressed α- and γ-phases.

4.2. Precipitate

Precipitate scattering was measurable for samples aged 30 min and longer times. This data enabled a comparison to be made between the precipitate size and shape determination, obtained by fitting the matrix scattering from field considerations. For both 15 and 30 min samples, the scattering from the thin dimension of the precipitate produced [0 0 1] streaks in long-term exposures of electron diffraction photographs. These broad modulations introduced background under the much sharper peaks shown in Fig. 3a. The sharp peaks, in the region measured, originated either from the large dimension of the continuous precipitate, from the discontinuous γ^1 or the beryllide peaks. Both of the latter are much larger in size than the dimensions of the continuous precipitate. The sharpness of the former peaks from continuous precipitates allowed Equation 3 to be applied without a cross-term correction. That is, Equation 12 could be applied directly, with the shape of the scattering determined by the Fourier series.

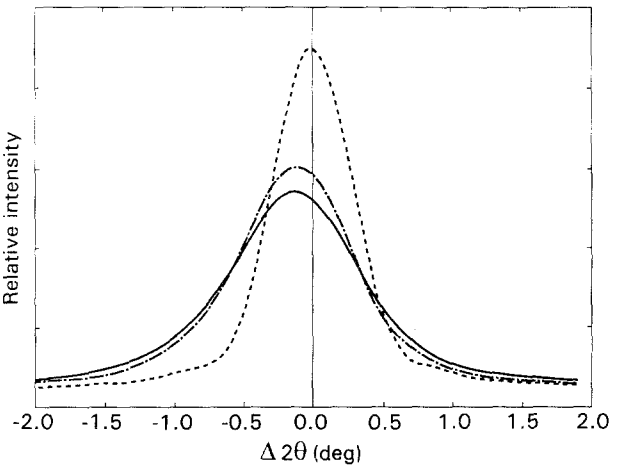

Figure 7 Precipitate scattering profiles from 30 min data (– – –) includes particle size, (– · –) includes particle size and strain, (——) includes particle size, strain and instrumental [30].

In applying the Fourier series to the 30 min data, the particle size term (N_n/N_3) was calculated for a flattened ellipsoid along the (1 0 0) habit plane. Also, the coefficients containing displacements, exp $\phi(n)$, were the same as those found in the matrix. In other words, displacements originating in the matrix were assumed to be continuous from matrix to precipitates. To make a comparison with the measured data, the Fourier series of Equation 12 was convoluted with the instrumental broadening which was taken to be the same as the nearby (1 0 0) beryllide peak. The various contributions are illustrated in Fig. 7. If both the strain field and instrumental broadening are included, the calculated FWHM is between 1.1 to 1.2 in Δ2θ°. This should be compared with a measured width of 1.49°. Although this difference may appear to be small it is real and other factors must be influencing the broadening of the precipitate scattering which have not been considered. A small monoclinic distortion of the tetragonal unit cell or interface dislocations would introduce additional broadening.

5. Discussion

These results are in agreement with the prediction that γ″ and γ′ are elastically distorted versions of γ. In its stress-free state, γ has the B2 structure with cubic axes of 0.2697 nm. The so called GP zone could be considered as a monolayer of B2 cells which contains Be atoms as a central layer and adjacent (0 0 1) layers that are Cu-rich. γ″ is a thicker version of the GP described as having the same {1 0 0} habit plane. The experimental equivalent stress-free transformation strains indicates that the layer of B2 cells were uniformly expanded with a fractional change of ca. 0.12 within the {1 0 0} habit planes beyond that found in the fcc matrix. This gave a major contraction in the perpendicular direction of ca. – 0.35, which was larger than the Bain strain calculated from the stress-free lattice parameters of the matrix and γ according to Equation 13. At this point, one must consider exactly what lattice parameters are to be used in calculating the Bain strain. Khachaturyan and Laughlin used a matrix

lattice parameter very close to pure Cu. If the transformation proceeds by a matrix enrichment to ca. 50 at % Be per unit cell, and a Bain strain is subsequently imposed on an interior bcc cell within a fcc matrix, one obtains a different estimate of the Bain strain. Without lattice parameter data for the 50 at % Be fcc solution a Vegards Law extrapolation must be used. This can be done according to the volume of the unit cells with

$$a_i^3 = n_i V_{Cu} [1 + V_{SF} X_B] \quad (15)$$

where a_i designates the cell edge of either the fcc matrix ($i = M$) or the γ-phase ($i = \gamma$). If one estimates the lattice parameter of γ, with two atoms/cell ($n_\gamma = 2$) a value of 0.2737 nm is found using Vegards Law and the parameters $V_{Cu} = 0.01181$ nm^3 and $V_{SF} = -0.2645$, as listed by King [36]. This differs from the reported value 0.27 nm by + 1.4%. Introducing Vegards Law into Equation 13 for both structures gives $\varepsilon_{11} = \varepsilon_{22} = 0.122$ and $\varepsilon_{33} = -0.377$. These were determined entirely by geometrical considerations, since terms containing V_{Cu} and V_{SF} cancel when Equation 13 is applied for the 50 at % extrapolation. This represents an interesting result since both sets of equivalent transformation strains, obtained at 15 and 30 min, are within experimental error of the predicted extrapolated values. However, it is important to recall that these strains determine the displacement field in the matrix.

An examination of the apparent transformation strains in the precipitate gave different results. This is to be expected since it has different elastic constants and, in fact, may not be purely elastic in behaviour. The strain along the habit plane can be calculated for the 30 min sample. By taking $a_{\gamma''}(30) = 0.2577$ nm from Table I and $a_M = 0.3448$ nm from Vegards Law, one finds that $\varepsilon_{11} = \varepsilon_{22} = 0.057$ and $\varepsilon_{33} = -0.246$ at 50 at % Be. The values are intermediate, but if the full transformation to γ were examined, the strains would correspond to the equivalent transformation strains reported for the matrix. Since the precipitate peaks shifted continuously, the transformation strains for the precipitate changed continuously, and appeared to be particularly size dependent.

Although the precipitate peaks shifted continuously, the sharp Bragg peaks from the matrix did not show a similar shift. This requires that the volume associated with each Be atom must remain unchanged as it transfers from the matrix to a site in a precipitate. In other words, there is no observable relaxation process associated with the transfer to either a GP zone or to γ''. During the transformation associated with γ' the quasilines shifted and some relaxation was likely to be occurring.

The tetragonal transformation strain imposed on the transformed zone produced severe displacements in the surrounding matrix, having an inverted tetragonal symmetry with respect to the precipitate, i.e. an expansion perpendicular to the disc and contraction within the plane. The major diameter increased from ca. 0.90 to 20.0 nm in going from the GP zone to γ'', and the thickness increased from a monolayer of distorted B2 cells to a double layer. This is in accord with results already reported in the literature [26, 27]. Both GP and γ'' precipitates produce severe matrix distortions, seen in the matrix scattering as a dominance of quasilines.

The results are in general agreement with the theory proposed by Khachaturyan and Laughlin that yielded γ'' and γ' by way of an elastic distortion of γ. However, these results show differences in the predicted a_γ^P and b_γ^P parameters for γ'. b_γ^P was assumed to be constant at 0.2554 nm. Instead the precipitate peaks shifted continously toward a position corresponding to stress-free γ with a lattice parameter of ca. 0.27 nm. An examination of the apparent average particle sizes from a Scherrer calculation show that the present values are almost an order of magnitude too small for the precipitate diameter. A monoclinic precipitate lattice would account for this discrepancy. However, the difference $a_\gamma^P - b_\gamma^P$ as predicted by KL theory is about a factor of two too large to agree with the line broadening data. After 24 h at 315 °C, a_γ^P could be at or slightly smaller than 0.27 nm while b_γ^P ca. 0.26 nm, could not be a constant.

Throughout the transformation to γ' the matrix lines continued to appear as quasilines. This suggests that the matrix remained severely distorted. Although this stage has not been modelled quantitatively, the combined sharpening and some systematic shifting in peak position would suggest that some relaxation of strain was occurring which was not apparent with the transformation to γ''. This correlates with the disappearance of striations from electron microscopy.

Finally, although the transformation was examined over a considerable time range (15 min to 168 h), which extended over the hardness maximum, no significant change was found for the fraction of matrix transformed. Rather, these results can be interpreted as a coarsening process. That is, enriched regions grew at the expense of those of a smaller size. Of course, this growth and related deformation in the matrix play an important role in determining maximum hardness.

Acknowledgements

Funding for this research was made available by National Science Grant No. DMR-8818013. The author is grateful to Dr Amitava Guha (Brush Wellman Inc., Cleveland, OH) for providing samples and his preliminary discussions that provided a very useful background for this research.

References

1. A. GUINIER and P. JACQUET, *Rev. Met.* **41** (1944) 1.
2. A. G. GUY, C. S. BARRETT and R. F. MEHL, *Trans. Met. Soc. AIME* **175** (1948) 216.
3. W. GRUHL and G. WASSERMANN, *Metall.* **5** (1955) 141.
4. A. H. GEISLER, J. H. MALLERY and F. E. STEIGERT, *Trans. Met. Soc. AIME* **194** (1952) 307.
5. YU. D. TYAPKIN and A. V. GAVRILOVA, *Sov. Phys. (Crystallog.)* **9** (1964) 166.
6. YU. D. TYAPKIN, *ibid.* **10** (1966) 418.
7. A. SAULNIER and P. MIRAND, *Rev. Met.* **57** (1960) 91.
8. K. TANAKA, M. MANNAMI and K. IZUMI, *Acta Metall.* **11** (1963) 79.
9. R. J. PRICE and A. KELLY, *ibid.* **11** (1963) 915.

10. W. K. ARMITAGE, PhD Thesis, University of Leeds, Leeds, UK (1963).
11. M. NAKAGAWA, *Jpn J. Appl. Phys.* **4** (1965) 760.
12. I. PFEIFFER, *Z. Metallk.* **56** (1965) 465.
13. A. M. ELISTRATOV and L. M. SOROKIN, *Sov. Phys. (Solid State)* **6** (1965) 24.
14. L. E. TANNER, *Phil. Mag.* **14** (1966) 111.
15. L. M. SOROKIN, *Sov. Phys. (Solid State)* **8** (1967) 2820.
16. *Idem., ibid.* **9** (1967) 1353.
17. A. V. GAVRILOVA, YU. D. TYAPKIN and M. P. USIKOV, *Sov. Phys. (Doklady)* **12** (1968) 970.
18. Z. HENMI and T. NAGAI, *Trans. Jpn Inst. Met.* **10** (1969) 166.
19. P. WILKES and M. M. JACKSON, *Met. Sci. J.* **3** (1969) 130.
20. V. A. PHILLIPS and L. E. TANNER, *Acta Metall.* **21** (1973) 441.
21. S. YAMAMOTO, M. MATSUI and Y. MURAKAMI, *Trans. Jpn Inst. Met.* **12** (1971) 159.
22. K. SHIMIZU, Y. MIKAMI, H. MITANI and K. OTSUKA, *ibid.* **12** (1971) 206.
23. Y. MURAKAMI, H. YOSHIDA and S. YAMAMOTO, *Trans. Jpn Inst. Met.* **9** (1968) 11.
24. A. R. ENTWISLE and J. K. WYNN, *J. Inst. Metals* **89** (1960) 24.
25. W. BONFIELD, *Trans. Met. Soc. AIME* **239** (1967) 99.
26. W. BONFIELD and B. C. EDWARDS, *J. Mater. Sci.* **9** (1974) 398, 409, 415.
27. R. J. RIOJA and D. E. LAUGHLIN, *Acta Metall.* **28** (1980) 1301.
28. A. G. KHACHATURYAN and D. E. LAUGHLIN, *Acta Metall. Mater.* **38** (1990) 1823.
29. B. HE, PhD Thesis, Virginia Polytechnic Institute and State University (1992).
30. C. H. WU, PhD Thesis, Virginia Polytechnic Institute and State University (1993).
31. C. R. HOUSKA, *Acta Cryst.* **A49** (1993) 771.
32. B. D. CULLITY, "Elements of X-ray diffraction" (Addison-Wesley, Reading, MA, 1978).
33. B. E. WARREN, "X-ray diffraction" (Addison-Wesley, Reading, MA, 1969).
34. J. E. LEE, D. M. BARNETT and H. I. AARONSON, *Met. Trans. A* **8A** (1977) 963.
35. M. A. KRIVOGLAZ, "Theory of X-ray and thermal-neutron scattering by real crystals" (Plenum, NY, 1969).
36. H. W. KING, *J. Mater. Sci.* **1** (1966) 79.
37. G. SIMMONS and H. WANG, "Single crystal elastic constants and calculated aggregate properties: A handbook" (MIT Press, Cambridge, MA, 1971).
38. D. J. CHAKRABARTI, D. E. LAUGHLIN and L. E. TANNER, *Bull. Alloy Phase Dia.* **8** (1987) 269.

Received 14 September 1993
and accepted 10 January 1994